

The Galactic Bulge exploration I.: The period-absolute magnitude-metallicity relations for RR Lyrae stars for G_{BP} , V , G , G_{RP} , I , J , H , and K_s passbands using *Gaia* DR3 parallaxes

Z. Prudil^{1,2}, A. Kunder³, I. Dékány¹, A. J Koch-Hansen¹

¹ Astronomisches Rechen-Institut, Zentrum für Astronomie der Universität Heidelberg, Mönchhofstr. 12-14, D-69120 Heidelberg, Germany

² European Southern Observatory, Karl-Schwarzschild-Strasse 2, 85748 Garching bei München, Germany; e-mail: Zdenek.Prudil@eso.org

³ Saint Martin's University, 5000 Abbey Way SE, Lacey, WA, 98503

October 31, 2023

ABSTRACT

We present a new set of period–absolute magnitude–metallicity (PMZ) relations for single-mode RR Lyrae stars calibrated for the optical G_{BP} , V , G , G_{RP} , near-infrared I , J , H , and K_s passbands. We compiled a large dataset (over 100 objects) of fundamental and first-overtone RR Lyrae pulsators consisting of mean intensity magnitudes, reddenings, pulsations properties, iron abundances, and parallaxes measured by the *Gaia* astrometric satellite in its third data release. Our newly calibrated PMZ relations encapsulate the most up-to-date ingredients in terms of both data and methodology. They are aimed to be used in conjunction with large photometric surveys targeting the Galactic bulge, including the Optical Gravitational Lensing Experiment (OGLE), the Vista Variables in the Vía Láctea Survey (VVV), and the *Gaia* catalog. In addition, our Bayesian probabilistic approach provides accurate uncertainty estimates of the predicted absolute magnitudes of individual RR Lyrae stars. Our derived PMZ relations provide consistent results when compared to benchmark distances to Globular clusters NGC 6121 (also known as M4), NGC 5139 (also known as omega Cen), and Large and Small Magellanic Clouds, which are stellar systems rich in RR Lyrae stars. Lastly, our K_s -band PMZ relations match well with the previously published PMZ relations based on *Gaia* data and accurately predict the distance toward the prototype of this class of variables, the eponymic RR Lyr itself.

Key words. Stars: variables: RR Lyrae – methods: statistical – methods: data analysis – parallaxes

1. Introduction

RR Lyrae stars are old, helium-burning, mostly radially pulsating horizontal branch giants. They are divided into three main groups based on their pulsation mode; fundamental mode (RRab), first-overtone (RRc), and double-mode pulsators (RRd) pulsating both in fundamental and first-overtone mode. The pulsation properties of all three subclasses have been studied extensively (e.g., Bono et al. 1996; Szabó et al. 2010; Netzel et al. 2015; Smolec et al. 2015; Skarka et al. 2020; Molnár et al. 2022; Netzel & Smolec 2022). The fundamental mode RR Lyrae pulsators often serve as distance and metallicity indicators toward old stellar systems within our Galaxy (e.g., Braga et al. 2015; Skowron et al. 2016; Dékány et al. 2021) and beyond (e.g., Sarajedini et al. 2006, 2009; Fiorentino et al. 2012; Savino et al. 2022).

In particular, the connection between pulsation periods, absolute magnitudes, and metallicities (PMZ relations) of RR Lyrae stars allows us to infer their distances from photometric time series, and it has been one of their most practical features. RR Lyrae PMZ relations have granted opportunities to study structures of old stellar systems (e.g., Dékány et al. 2013; Martínez-Vázquez et al. 2016; Jacyszyn-Dobrzeńicka et al. 2017, 2020) and their distances (e.g., Braga et al. 2015; Martínez-Vázquez et al. 2019; Bhardwaj et al. 2020; Fabrizio et al. 2021; Bhardwaj et al. 2021).

There are both theoretical and empirical approaches to calibrate the PMZ relations in the literature for various passbands ranging from optical to far-infrared (e.g., Bono et al. 2003; Catelan 2004; Neeley et al. 2015; Marconi et al. 2015; Neeley et al. 2017; Marconi et al. 2018; Muraveva et al. 2018a; Neeley et al. 2019; Garofalo et al. 2022).

Empirical studies in the past relied on large samples of RR Lyrae stars (≈ 400) with metallicities on the Zinn & West (1984) metallicity scale (combining both spectroscopically and photometrically estimated metallicities, e.g., Dambis et al. 2013; Muraveva et al. 2018a; Muhie et al. 2021). The distances in the aforementioned studies were either based on statistical parallax analysis (e.g., Dambis 2009; Dambis et al. 2013) or on trigonometric parallaxes measured by the *Gaia* space mission (e.g., Muraveva et al. 2018a; Neeley et al. 2019; Layden et al. 2019; Muhie et al. 2021; Garofalo et al. 2022) or lastly using distances to RR Lyrae rich globular clusters (e.g., Neeley et al. 2015; Bhardwaj et al. 2021). The photometric information often came from various sources, mainly large photometric surveys covering a broad range of passbands.

In this work, we aim to empirically calibrate the PMZ relations for three major photometric surveys targeting (among others) dense stellar regions in the Milky Way; the Optical Gravitational Lensing Experiment (OGLE, Udalski et al. 2015), the

Vista Variables in the Vía Láctea survey (VVV, Minniti et al. 2010), and *Gaia* astrometric mission (Gaia Collaboration et al. 2016). The combination of these surveys provides optical (OGLE, *Gaia*) and near-infrared (VVV) photometry for tens of thousands of RR Lyrae stars in crowded stellar regions in the Milky Way. The precise calibration of PMZ relations will allow for accurate distance determination and possible avenues to treat extinction directly based on the color excess of RR Lyrae pulsators. This will enable us to probe the structure of the Galactic bulge from the point of view of old population pulsators (similarly to studies like Dékány et al. 2013; Pietrukowicz et al. 2015; Prudil et al. 2019a; Du et al. 2020; Molnar et al. 2022) and its kinematical properties (Kunder et al. 2016; Prudil et al. 2019b; Kunder et al. 2020; Du et al. 2020).

Previous studies have used both theoretical and empirical PMZ relations to determine distances toward the RR Lyrae population in the Galactic bulge. These relations were not directly calibrated to the photometric systems of OGLE and VVV. They required re-calibration mainly since the OGLE *V*-band is partially different from the standard Johnson *V*-passband (see Udalski et al. 2015), and also the VVV *JHK_s* passbands differ from those in the *Two-Micron Sky Survey* (2MASS, Cutri et al. 2003; Skrutskie et al. 2006). In addition, the metallicity term in the aforementioned PMZ relations was usually calibrated to a different metallicity scale than the estimated metallicities for the bulge RR Lyrae population, thus requiring further conversion (e.g., for *Gaia* photometry in a study by Muraveva et al. 2018a). Furthermore, previous studies of the Galactic bulge relied mostly on external extinction maps and did not use RR Lyrae stars themselves as tracers of extinction. This motivated the decision to provide PMZ relations that are more appropriate for RR Lyrae stars toward the Galactic bulge. Our subsequent papers will use this calibration to investigate the structure and kinematics of the bulge RR Lyrae population. For the newly derived PMZ relations, we used purely geometrically determined distances by the *Gaia* astrometric mission (Lindgren et al. 2021; Gaia Collaboration et al. 2022), combined with publicly available data on RR Lyrae stars in the Solar neighborhood. In particular, we aimed to use a homogenous metallicity scale among calibrating stars that will allow direct use of photometric metallicities derived from OGLE *I*-band photometry for RR Lyrae variables toward the Galactic bulge.

This paper is structured as follows: In Section 2, we describe our assembled dataset and analysis of the data. The subsequent Section 3 outlines our statistical approach to the PMZ calibration and derived equations together with their covariance matrices. In Sect. 4, we test our newly derived relation with the literature values for some of the RR Lyrae-rich stellar systems. Finally, Section 5 summarizes our results.

2. Dataset for calibration of the PMZ relations

We based our calibration sample on stars with iron abundances collected in Crestani et al. (2021a) and Dékány et al. (2021). Similar to the calibration by Dékány et al. (2021), individual spectroscopic measurements of [Fe I/H] and [Fe II/H] were collected from the literature and shifted to the common metallicity scale defined by For et al. (2011); Chadid et al. (2017); Sneden et al. (2017); Crestani et al. (2021b, abbreviated as CFCS) using offsets from Dékány et al. (2021). Each star in our calibration sample had multiple published iron abundance measurements and an associated uncertainty. We obtained the pulsation properties (pulsation period, P) for individual variables in the spectroscopic dataset

from various sources, mainly from the International Variable Star Index (VSX, Watson et al. 2006).

Often pulsation periods are quoted without their appropriate errors; thus, to account for possible minor uncertainties in P we used the following equation to approximate the uncertainties of pulsation periods σ_P :

$$\sigma_P = 1.001 \cdot P - 0.999 \cdot P \quad . \quad (1)$$

This approach fits σ_P over an approximate baseline of 1000 days. For a general RRab variable with a pulsation period equal to 0.5 day Eq. 1 yields $\sigma_P = 0.001$ day. In addition, we converted pulsation periods of the first-overtone (FO) pulsators into fundamental mode using the following equation from Iben & Huchra (1971) and Braga et al. (2016):

$$\log_{10}(P) = \log_{10}(P_{FO}) + 0.127 \quad . \quad (2)$$

For the entire spectroscopic dataset, values for parallaxes ϖ , and their uncertainties σ_ϖ , were obtained from the third data release (DR3) of the *Gaia* mission (and subsequently corrected for the zero point offset¹, by Lindgren et al. 2021). To account for interstellar reddening and to ensure its homogenous treatment, we used 2D extinction maps from Schlegel et al. (1998) to obtain $E(B - V)$ color excesses and its uncertainties toward individual stars and re-calibrated reddening laws from Schlafly & Finkbeiner (2011). The spatial distribution of our spectroscopic dataset in the Galactic coordinates is depicted in Fig. 1.

2.1. Mean intensity magnitudes

The intensity magnitudes were obtained from various sources and subsequently transformed into the OGLE and VVV passbands. We emphasize that our RR Lyrae sample sizes vary between the different passbands, and we list the final number of RR Lyrae stars for each calibration after applying quality cuts (see Section 3 and Eq. 15).

In the case of the G_{BP} , G and G_{RP} -bands photometry, we utilized the *Gaia* RR Lyrae catalog with their associated photometric and pulsation properties (Clementini et al. 2022). As the mean intensity magnitudes, $m_{G_{BP}}$, m_G , $m_{G_{RP}}$, we used intensity-averaged magnitudes in the aforementioned bands together with their RR Lyrae subclassification, pulsation periods, and uncertainties on pulsation periods. In total, we used 240 (201 RRab and 39 RRc stars) RR Lyrae variables for G_{BP} , G and G_{RP} -bands, respectively.

For the *V*-passband, we obtained photometry for RR Lyrae stars and subsequently their mean intensity magnitudes, m_V , from the All-Sky Automated Survey for Supernovae (ASAS-SN, Shappee et al. 2014; Jayasinghe et al. 2018). This sample contained 166 RR Lyrae stars (136 RRab and 30 RRc pulsators). The same match was conducted for the *I*-band photometry from Dékány et al. (2021), which yielded 128 RR Lyrae stars in total (104 RRab and 24 RRc pulsators) with mean intensity magnitudes m_I . We note that *I*-band photometry for the calibration RR Lyrae stars came from the predecessor of ASAS-SN, the All Sky Automated Survey (ASAS, Pojmanski 1997; Szczygiel et al. 2009) and was collected from work by Dékány et al. (2021).

The mean intensity magnitudes for *V* and *I*-passbands were obtained through Fourier decomposition of photometric light

¹ Using a code https://gitlab.com/icc-ub/public/gaidr3_zeropoint.

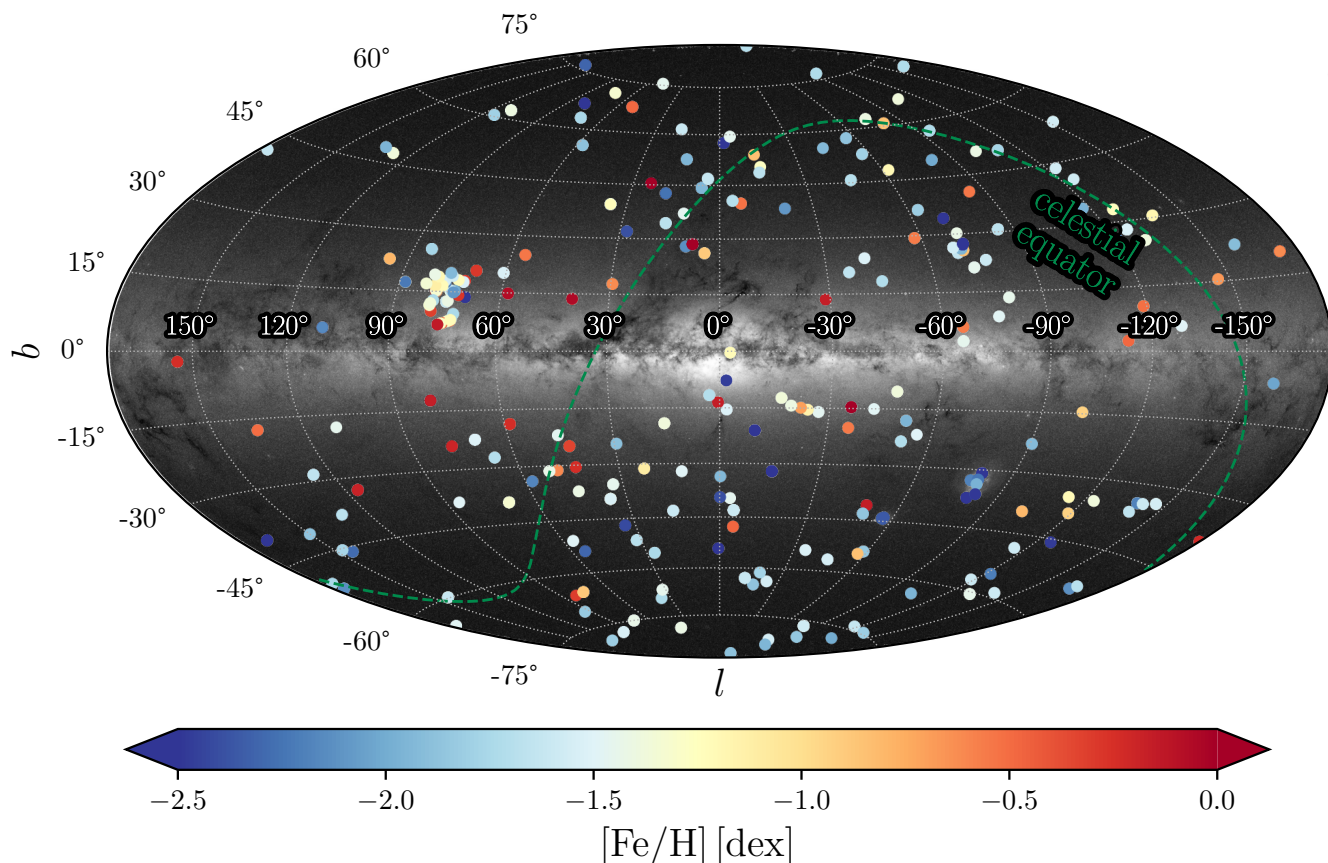


Fig. 1. Spatial distribution in the Galactic coordinates of our RR Lyrae calibration dataset with color-coding representing objects metallicity. *Gaia*'s all-sky star density map is underpinned in the background. The overdensity at $l \approx 80$ deg and $b \approx 10$ deg is due to RR Lyrae stars observed by the *Kepler* space telescope and followed up spectroscopically by Nemeč et al. (2013). Image credit: *Gaia* Data Processing and Analysis Consortium (DPAC); A. Moitinho / A. F. Silva / M. Barros / C. Barata, University of Lisbon, Portugal; H. Saviotto, Fork Research, Portugal.

curves using an approach described in Petersen (1986). We optimized the following Fourier light curve decomposition:

$$m(t) = m + \sum_{k=1}^n A_k \cdot \cos(2\pi k\vartheta + \varphi_k) \quad (3)$$

In Equation 3, m , represents the mean intensity magnitude, A_k and φ_k stand for amplitudes and phases. The n denotes the degree of the fit which we adapted for each light curve using the same approach as in Prudil et al. (2019a). The ϑ represents the phase function defined as:

$$\vartheta = (\text{HJD} - M_0) / P \quad (4)$$

where HJD is a Heliocentric Julian Date representing the time of the observation, and M_0 stands for the time of brightness maximum².

The V and I -passbands from the ASAS-SN and ASAS surveys were directly transformed into the OGLE photometric system (Udalski et al. 2015) using common stars between surveys. We used the following linear relations to transform intensity magnitudes:

$$m_V^{\text{OGLE}} = 1.003 \cdot m_V + 0.006 \quad (5)$$

$$m_I^{\text{OGLE}} = 0.992 \cdot m_I + 0.107 \quad (6)$$

² It is important to note, that the M_0 was estimated for each survey separately.

In the case of the J and H -bands, we used the photometry provided by the 2MASS and estimated mean intensity magnitudes, m_J and m_H , from Braga et al. (2019). Since 2MASS provides, in most cases, single epoch observations at different pulsation phases, we needed to correct for the luminosity variation during the pulsation cycle to obtain mean intensity magnitudes. For this purpose, we utilized near-infrared photometric templates derived by Braga et al. (2019) in combination with optical, V -band, photometric data from ASAS (to accurately estimate M_0 Pojman-ski 1997). The choice of using the ASAS data stemmed from the similar time baseline between ASAS and 2MASS, which allowed better constraints to the 2MASS single epoch observations (pulsation period, time of brightness maxima, amplitude) necessary for template fitting and obtaining the m_J and m_H . In the end, we had 115 RR Lyrae stars (97 RRab and 18 RRc variables) with mean intensity magnitudes m_J and 111 RR Lyrae stars (94 RRab and 17 RRc variables) with mean intensity magnitudes m_H .

The mean intensity magnitudes in K_s -band were acquired from several sources, particularly from studies by Layden et al. (2019) and Braga et al. (2019). We also used the 2MASS survey, where the same approach as in the J and H -passbands was used to correct for the luminosity variations as a function of the pulsation cycle. A combination of the studies and surveys mentioned earlier resulted in 155 RR Lyrae stars (129 RRab and 26 RRc variables) with mean intensity magnitudes m_{K_s} . The dataset provided by Layden et al. (2019) offered the mean K_s -band magnitudes transformed into the 2MASS photometric system, while Braga et al.

(2019) photometry was also calibrated to the 2MASS photometric system. Therefore, acquired J , H , and K_s mean intensity magnitudes needed to be transformed into the VVV photometric system. We used the equations from the CASU website³ and color terms $J - K_s$ for individual stars to convert our m_J , m_H , and m_{K_s} magnitudes into the VVV photometric system.

3. Calibration of the PMZ

In this work, we aim to improve the following relation:

$$M = \alpha \log_{10}(P) + \beta [\text{Fe}/\text{H}] + \gamma \quad , \quad (7)$$

where M is the absolute magnitude in the given passband (in our study G_{BP} , V , G , G_{RP} , I , J , H , and K_s). The pulsation periods and metallicities are denoted as P and $[\text{Fe}/\text{H}]$, together with parameters of the PMZ marked as α , β , and γ . Although our dataset is smaller in comparison to previous studies (e.g., [Dambis et al. 2013](#); [Muraveva et al. 2018a](#); [Muhie et al. 2021](#)), our calibration is based on a homogeneous metallicity scale that is the same as what is used for the Galactic bulge RR Lyrae stars. This allows for more accurate reddening and distance to be derived, especially in the G_{BP} , V , G , G_{RP} , and I -passbands which are more affected by both reddening and the effect of $[\text{Fe}/\text{H}]$ metallicity on absolute magnitude. It is important to emphasize that we used both pulsation periods and metallicities to estimate absolute magnitudes for optical (G_{BP} and V) passbands instead of only metallicities as was done in previous studies (e.g., [Catelan et al. 2004](#); [Muraveva et al. 2018a](#)). We used both based on a mild anticorrelation (Pearson correlation coefficient equal to -0.47) between pulsation periods and absolute magnitudes (calculated using parallaxes), for both passbands. In addition, the combination of both parameters will decrease uncertainty in the distance, particularly in cases where the metallicity of a given RR Lyrae variable is unknown or highly uncertain.

Our dataset for each passband \mathbf{D} consists of vectors \mathbf{d}^k that contain the following information for individual stars k :

$$\mathbf{d}^k = \{\log_{10}(P), [\text{Fe}/\text{H}], \varpi, m, E(B - V)\}^k \quad . \quad (8)$$

To properly account for errors in our catalog and accurately estimate the PMZ parameters, we employed the following approach utilizing the Bayesian framework where the posterior probability $p(\theta | \mathbf{D})$ is equal to:

$$p(\theta | \mathbf{D}) \propto p(\mathbf{D} | \theta) p(\theta) \quad . \quad (9)$$

The θ represents the model parameters $\theta_i = \{\alpha_i, \beta_i, \gamma_i, \varepsilon_{M_i}\}$ of the PMZ relation (see equation 7), ε_{M_i} represents the intrinsic scatter in the PMZ relation, and the $p(\theta)$ is the prior probability of the parameter set θ . In our approach, we assumed the prior probability for the intrinsic scatter in the PMZ, ε_M , that was in the form of a Jeffreys log-uniform prior ([Jaynes 1968](#)):

$$p(\varepsilon_{M_i}) = 1/\varepsilon_{M_i} \quad . \quad (10)$$

For the α , β , and γ parameters we selected mildly informative uniform priors, \mathcal{U} , based on values from [Marconi et al. \(2015\)](#), see their Table 6 for I , J , H , and K_s). We used the following priors for both the optical G_{BP} , V , G , and G_{RP} bands:

$$p(\alpha_i, \beta_i, \gamma_i) = \mathcal{U}(-2.5 < \alpha < 0.5) \quad (11)$$

$$\mathcal{U}(0.0 < \beta < 0.5) \quad (12)$$

$$\mathcal{U}(-1.5 < \gamma < 1.5) \quad . \quad (13)$$

³ <http://casu.ast.cam.ac.uk/surveys-projects/vista/technical/photometric-properties/sky-brightness-variation/view>

The marginalized likelihood $p(\mathbf{D} | \theta)$ for k number of stars can be written as such:

$$p(\mathbf{D} | \theta_i) = \prod_{k=1}^K p(\mathbf{d} | \theta) = \prod_{k=1}^K \mathcal{N}(M_{\text{data}} | M_{\text{model}}, \sigma_{M_{\text{tot}}}) \quad , \quad (14)$$

The M_{data} represents absolute magnitudes estimated using collected photometric and astrometric data. The M_{model} stands for absolute magnitudes estimated through Eq. 7. The \mathcal{N} represents the normal distribution with a mean μ and standard deviation σ for a variable x , $\mathcal{N}(x | \mu, \sigma^2)$. In the equations above, R_i denotes the extinction coefficient in a given passband, where we selected a baseline from [Cardelli et al. \(1989\)](#) with $R_V = 3.1$, for individually calibrated passband, we used extinction coefficients from [Schlafly & Finkbeiner \(2011\)](#), for V , I , and K_s , and for the *Gaia* G_{BP} , G , and G_{RP} -passbands we used the color-dependent extinction coefficients from [Gaia Collaboration et al. \(2018\)](#), see their Eq. 1 and Table 1 for details). The total uncertainty, $\sigma_{M_{\text{tot}}}$, encompassed the individual uncertainties for M_{data} , M_{model} and ε_{M_i} added in quadrature.

We implemented a set of selection criteria for all involved passbands to ensure we use high-quality data. The general requirements on RR Lyrae stars used for PMZ calibration were that re-normalized unit weight error (RUWE⁴) was lower than 1.4, uncertainty on mean intensity magnitude was $\sigma_{m_i} < 0.1$ mag, and we used only stars outside the highly reddened regions of the MW using condition $|b| > 15$ deg. The first and third general conditions prevented the possible problems with astrometric and photometric solutions (e.g., blending). The second condition was primarily applied in order to uncertain mean intensity magnitudes in J . In addition, we implemented two conditions on parallax significance and reddening:

$$\varpi/\sigma_{\varpi} > 20 \quad \text{and} \quad E(B - V) < 0.3 \quad . \quad (15)$$

These conditions ensured that we used highly precise parallaxes with stars only weakly affected by reddening. The latter was particularly important for optical passbands where reddening and selecting a reddening law could play a significant role in PMZ calibration.

Using the aforementioned approach and selection criteria, we proceeded to estimate the parameters of the individual PMZ relations. To explore the parameter space, θ , we employed the Markov Chain Monte Carlo Ensemble sampler implemented in the EMCEE package [Foreman-Mackey et al. \(2013\)](#) to maximize the posterior probability defined in the Eq. 9. We ran EMCEE with 100 walkers for 5000 steps. Using EMCEE we thinned the chains by $\tau = 10$ and selected the first 4000 steps as a burn-in, which resulted in 10000 samples for the posterior distributions. The distribution of θ parameters for K_s , H , J , I , G_{RP} , G , G_{BP} , and V -bands is shown in Figures 2, A.1, A.2, A.3, A.4, A.5, A.7, and A.6, respectively. The parameters of PMZ relations for eight passbands, together with the total number of variables, N , used

⁴ The RUWE parameter estimates the quality of the *Gaia* astrometric solution.

in calibration, can be found in the following equations:

$$M_{K_s} = -2.342 \log_{10}(P) + 0.138 [\text{Fe}/\text{H}] - 0.801, N = 97 \quad (16)$$

$$M_H = -2.250 \log_{10}(P) + 0.157 [\text{Fe}/\text{H}] - 0.665, N = 72 \quad (17)$$

$$M_J = -1.799 \log_{10}(P) + 0.160 [\text{Fe}/\text{H}] - 0.378, N = 64 \quad (18)$$

$$M_I = -1.292 \log_{10}(P) + 0.196 [\text{Fe}/\text{H}] + 0.197, N = 79 \quad (19)$$

$$M_{G_{\text{RP}}} = -1.464 \log_{10}(P) + 0.167 [\text{Fe}/\text{H}] + 0.113, N = 110 \quad (20)$$

$$M_G = -0.950 \log_{10}(P) + 0.202 [\text{Fe}/\text{H}] + 0.614, N = 110 \quad (21)$$

$$M_V = -0.582 \log_{10}(P) + 0.224 [\text{Fe}/\text{H}] + 0.890, N = 112 \quad (22)$$

$$M_{G_{\text{BP}}} = -0.593 \log_{10}(P) + 0.228 [\text{Fe}/\text{H}] + 0.913, N = 107 \quad (23)$$

Their covariance matrices with associated intrinsic scatter are the following:

$$\text{Cov}_{K_s} = \begin{bmatrix} \sigma_{\alpha_{K_s}} & \sigma_{\beta_{K_s}} & \sigma_{\gamma_{K_s}} \\ 0.00287 & 0.00017 & 0.00113 \\ 0.00017 & 0.00008 & 0.00017 \\ 0.00113 & 0.00017 & 0.00062 \end{bmatrix} \quad \varepsilon_{M_{K_s}} = 0.092 \quad (24)$$

$$\text{Cov}_H = \begin{bmatrix} \sigma_{\alpha_H} & \sigma_{\beta_H} & \sigma_{\gamma_H} \\ 0.01007 & 0.00052 & 0.00375 \\ 0.00052 & 0.00030 & 0.00062 \\ 0.00375 & 0.00062 & 0.00216 \end{bmatrix} \quad \varepsilon_{M_H} = 0.151 \quad (25)$$

$$\text{Cov}_J = \begin{bmatrix} \sigma_{\alpha_J} & \sigma_{\beta_J} & \sigma_{\gamma_J} \\ 0.01397 & 0.00049 & 0.00476 \\ 0.00049 & 0.00041 & 0.00081 \\ 0.00476 & 0.00081 & 0.00275 \end{bmatrix} \quad \varepsilon_{M_J} = 0.171 \quad (26)$$

$$\text{Cov}_I = \begin{bmatrix} \sigma_{\alpha_I} & \sigma_{\beta_I} & \sigma_{\gamma_I} \\ 0.00496 & 0.00027 & 0.00200 \\ 0.00027 & 0.00016 & 0.00033 \\ 0.00200 & 0.00033 & 0.00118 \end{bmatrix} \quad \varepsilon_{M_I} = 0.112 \quad (27)$$

$$\text{Cov}_{G_{\text{RP}}} = \begin{bmatrix} \sigma_{\alpha_{G_{\text{RP}}}} & \sigma_{\beta_{G_{\text{RP}}}} & \sigma_{\gamma_{G_{\text{RP}}}} \\ 0.00348 & 0.00019 & 0.00135 \\ 0.00019 & 0.00009 & 0.00019 \\ 0.00135 & 0.00019 & 0.00072 \end{bmatrix} \quad \varepsilon_{M_{G_{\text{RP}}}} = 0.107 \quad (28)$$

$$\text{Cov}_G = \begin{bmatrix} \sigma_{\alpha_G} & \sigma_{\beta_G} & \sigma_{\gamma_G} \\ 0.00432 & 0.00023 & 0.00166 \\ 0.00023 & 0.00011 & 0.00024 \\ 0.00166 & 0.00024 & 0.00089 \end{bmatrix} \quad \varepsilon_{M_G} = 0.118 \quad (29)$$

$$\text{Cov}_V = \begin{bmatrix} \sigma_{\alpha_V} & \sigma_{\beta_V} & \sigma_{\gamma_V} \\ 0.00564 & 0.00032 & 0.00220 \\ 0.00032 & 0.00015 & 0.00032 \\ 0.00220 & 0.00032 & 0.00119 \end{bmatrix} \quad \varepsilon_{M_V} = 0.140 \quad (30)$$

$$\text{Cov}_{G_{\text{BP}}} = \begin{bmatrix} \sigma_{\alpha_{G_{\text{BP}}}} & \sigma_{\beta_{G_{\text{BP}}}} & \sigma_{\gamma_{G_{\text{BP}}}} \\ 0.00498 & 0.00027 & 0.00192 \\ 0.00027 & 0.00013 & 0.00028 \\ 0.00192 & 0.00028 & 0.00104 \end{bmatrix} \quad \varepsilon_{M_{G_{\text{BP}}}} = 0.126 \quad (31)$$

In the derived PMZ relations, we see a linear dependence of individual coefficients and passbands. As we move from near-infrared toward the optical passband, the value of the α coefficient decreases (consequently the importance of pulsation period, Longmore et al. 1986; Dall’Ora et al. 2004), and the value of β increases (the relevance of metallicity). These effects are well known, particularly on the theoretical side, where the near-infrared K_s is shown to have less dependence on metallicity and also less dependence on evolutionary effects (see, e.g., Bono et al. 2003; Catelan et al. 2004; Marconi et al. 2015, 2018). Observations also indicate that there is a decrease in intrinsic scatter when finding M_{K_s} (e.g., Neeley et al. 2019; Layden et al. 2019; Cusano et al. 2021).

Together with the assumed intrinsic scatter in the PMZ, ε_M the absolute magnitude uncertainty calculation for a given RR Lyrae with a parameter vector $\mathbf{v} = \{\log_{10}(P), [\text{Fe}/\text{H}], 1.0\}$ is in the following form:

$$\sigma_M^2 = \mathbf{v} \times \text{Cov} \times \mathbf{v}^T + [\sigma_P \cdot \alpha / (P \log(10))]^2 + (\beta \cdot \sigma_{[\text{Fe}/\text{H}]})^2 + \varepsilon_M^2 \quad (32)$$

Comparison between absolute magnitude predictions based on our new PMZ relations and estimated absolute magnitudes calculated using *Gaia* parallaxes and dereddened intensity mean magnitudes are shown in Figures 3, A.9, A.10, A.12, and A.13.

4. Testing predicted absolute magnitudes and comparison of PMZ relations

In the following section, we examined the derived PMZ relations using the publicly available data on stellar systems with precisely derived distances using methods other than RR Lyrae PMZ relations. Also, we compare the derived relation for PMZ in K_s -band with those derived in the literature.

4.1. On the predicted absolute magnitudes

We selected only systems with a significant number of RR Lyrae stars and metallicities for testing predicted absolute magnitudes on the same metallicity scale as in our PMZ calibration. We picked globular clusters NGC 6121 and NGC 5139 (\equiv M 4 and ω Centauri, respectively) that have distances and their uncertainties derived using the *Gaia* parallaxes (Vasiliev & Baumgardt 2021, $\varpi^{\text{NGC}6121} = 0.556 \pm 0.010$ mas and $\varpi^{\text{NGC}5139} = 0.193 \pm 0.009$ mas, respectively). These distances are in agreement within two sigmas with the estimates based on RR Lyrae pulsators (Neeley et al. 2015; Braga et al. 2018). We used available mean intensity magnitudes in optical and near-infrared passbands from Stetson et al. (2014); Braga et al. (2016, 2018)

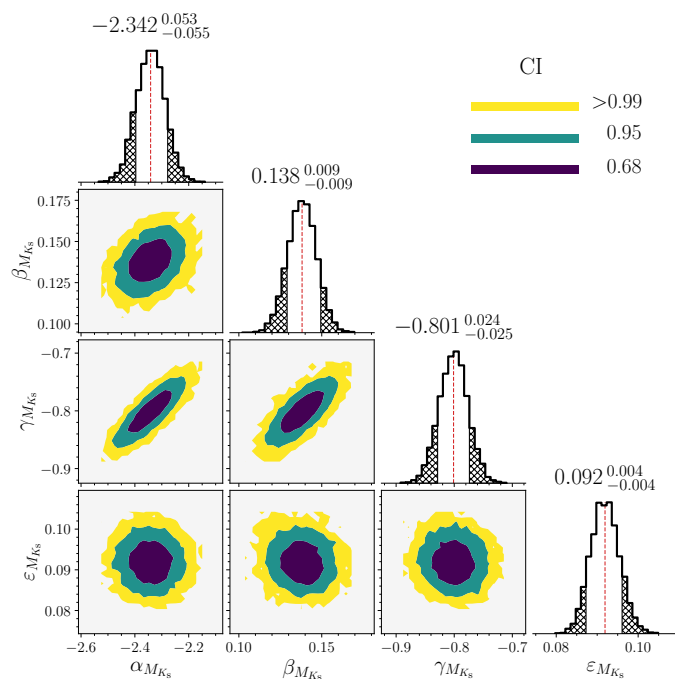


Fig. 2. Posterior probability distributions of the parameters of the PMZ relation for the K_s -passband.

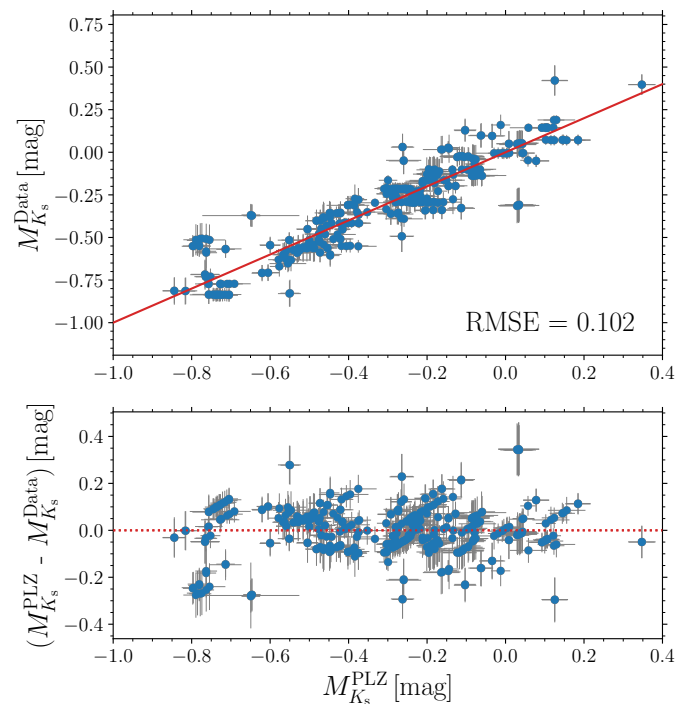


Fig. 3. Comparison of the absolute magnitudes predicted by our K_s -band PMZ relation with absolute magnitudes calculated based on *Gaia* data.

and their listed spectroscopic metallicities and pulsation periods when available. In the case of NGC 6121, we used a value for metallicity from Carretta et al. (2009) catalog since it is very close to the CFCS scale (difference below -0.1 dex, Crestani et al. 2021b). To account for extinction, we used reddening maps and reddening laws from Schlegel et al. (1998) and Schlafly & Finkbeiner (2011), respectively.

In the case of the Large and Small Magellanic Clouds (from hereon LMC and SMC), we used *Gaia* and OGLE-IV photometry (G_{BP} , V and I -bands), and stellar classifications from OGLE-IV (Soszyński et al. 2016). We re-analyzed the OGLE photometry using the Eq. 3 and estimated photometric metallicities using relations from Dékány et al. (2021), which are on the same scale as our PMZ calibration. For the near-infrared data, we obtained K_s mean intensity magnitudes for 8599 LMC RR Lyrae stars (Cusano et al. 2021) and 473 SMC RR Lyrae pulsators from Muraveva et al. (2018b). For the LMC and SMC distances, we used estimates from Pietrzyński et al. (2019) and Graczyk et al. (2020) based on late-type eclipsing binary stars. For dereddening the obtained mean intensity magnitudes, we used reddening maps from Schlegel et al. (1998) and reddening laws from Schlafly & Finkbeiner (2011).

We calculated the distance moduli of individual stars and estimated the peak of the distance modulus distribution for each system and passband using the Kernel density estimate routine (KDE, implemented in the *scipy* library, Virtanen et al. 2020). The error is estimated as the dispersion of the distance modulus distribution. It is worth noting that this method may not be ideal for the SMC and LMC, as they possess a significant depth extent that can lead to an increased level of measured distance dispersion (e.g., Jacyszyn-Dobrzyniecka et al. 2017; Tatton et al. 2021). In Figure 4, we compare our PMZ relations with distances to known stellar systems rich in RR Lyrae with sufficient data coverage. In general, the calculated distances using the absolute magnitude relations presented here mostly agree within one σ of the literature distance when using the optical G_{BP} , V , G , G_{RP} , I , and near-infrared J , H , and K_s passbands. The determined distance moduli are listed in Table 1 together with their literature values. In the case of the optical G_{BP} and G -bands, we see a significant offset (around $0.2 - 0.25$ mag) in distance modulus from the literature value for NGC 6121. This discrepancy is most likely caused by a significant differential reddening toward NGC 6121 (on average $E(B - V) = 0.5$ mag), the actual proximity of NGC 6121 (2D reddening maps provide only projected reddening), and in part, color-dependent extinction coefficients for G_{BP} and G -bands. The offset mostly disappears when we use 3D extinction maps (Green 2018; Green et al. 2019). In addition, the offset in the aforementioned optical bands is only observed for NGC 6121. In the other three comparisons, we see a good agreement with the literature distance moduli.

In conclusion, our optical and near-infrared PMZ relations agree with literature values for NGC 6121, NGC 5139, LMC, and SMC distances. We detect an offset from the canonical values that various effects, e.g., reddening, can cause for the G_{BP} and G -passbands.

4.2. Comparison with earlier studies

We compare our derived PMZ relation in the K_s -band with relations derived in different studies (e.g., Bono et al. 2003; Sollima et al. 2006, 2008; Borissova et al. 2009; Dambis et al. 2013; Muraveva et al. 2015; Bhardwaj et al. 2021; Muhie et al. 2021; Bhardwaj et al. 2023). We focused only on the PMZ in K_s -band due to the plethora of derived relations in the literature. We selected relations that combined pulsation periods and metallicities to obtain absolute magnitude in K_s -band.

In the end, we collected 15 relations from the literature for the determination of M_{K_s} , derived from both empirical and theoretical approaches. Figure 5 shows a comparison of the literature with the values presented here. Our derived coefficient for the pulsation period, α_{K_s} , matches quite well with the overall dis-

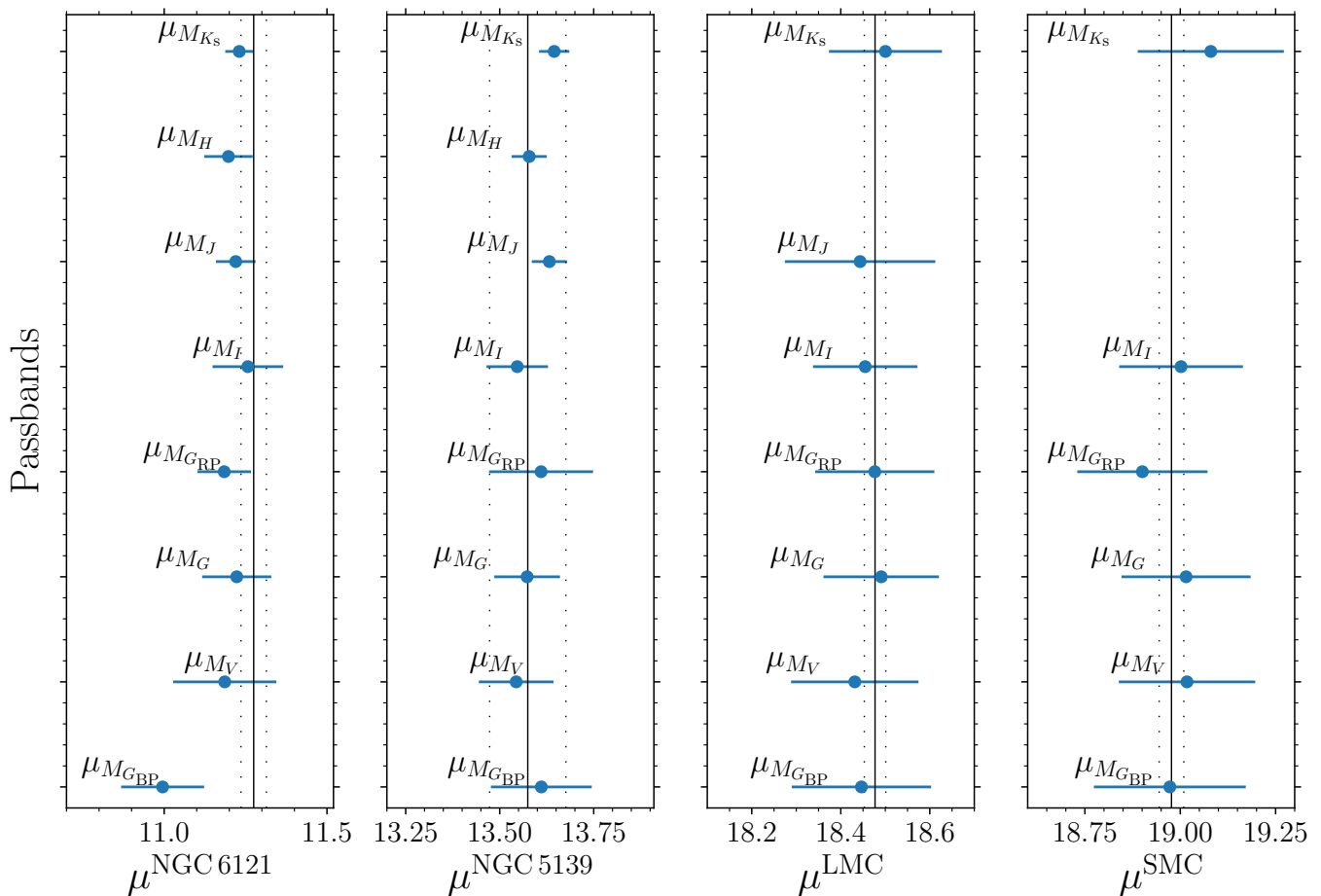


Fig. 4. Comparison of distance moduli for four systems (NGC 6121, NGC 5139, LMC, and SMC) with precise distances and uncertainties derived using different methods (other than RR Lyrae PMZ relations, Pietrzyński et al. 2019; Graczyk et al. 2020; Vasiliev & Baumgardt 2021). From the left, the plots show a comparison for globular clusters NGC 6121, NGC 5139, LMC, and SMC, using distances and their uncertainties depicted with solid and dotted black lines in all three plots.

Table 1. List of distance moduli for tested stellar systems using derived PMZ relations. The first column contains the source for calculated distance moduli (passbands and literature value). The second and third columns represent the distance moduli of two globular clusters, NGC 6121 and NGC 5139. The last two columns list distance moduli for Magellanic Clouds.

| Band | $\mu^{\text{NGC 6121}}$ [mag] | $\mu^{\text{NGC 5139}}$ [mag] | μ^{LMC} [mag] | μ^{SMC} [mag] |
|-----------------|----------------------------------|----------------------------------|-----------------------------|-----------------------------|
| G_{BP} | 11.00 ± 0.13 | 13.61 ± 0.13 | 18.45 ± 0.16 | 18.97 ± 0.20 |
| V | 11.25 ± 0.16 | 13.54 ± 0.10 | 18.43 ± 0.14 | 19.02 ± 0.18 |
| G | 11.12 ± 0.11 | 13.57 ± 0.09 | 18.49 ± 0.13 | 19.02 ± 0.17 |
| G_{RP} | 11.17 ± 0.08 | 13.61 ± 0.14 | 18.48 ± 0.13 | 18.90 ± 0.17 |
| I | 11.26 ± 0.11 | 13.55 ± 0.08 | 18.45 ± 0.12 | 18.91 ± 0.16 |
| J | 11.24 ± 0.06 | 13.63 ± 0.05 | 18.44 ± 0.17 | – |
| H | 11.16 ± 0.07 | 13.58 ± 0.05 | – | – |
| K_s | 11.27 ± 0.04 | 13.65 ± 0.04 | 18.50 ± 0.13 | 19.08 ± 0.19 |
| Lit. | 11.28 ± 0.04 | 13.58 ± 0.10 | 18.48 ± 0.02 | 18.98 ± 0.03 |

tribution of literature values. A similar conclusion can be made for the metallicity term, β_{K_s} , where despite different metallicity scales used in different studies (e.g., Zinn & West 1984; Carretta et al. 2009) we see a good agreement with the recent studies. Lastly, for the zero-point of the PMZ relations, γ_{K_s} , we see that our derived value agrees exceptionally well with the most recent

studies based on *Gaia* parallaxes despite various sources and scales of metallicity for these studies.

4.3. Comparison with the RR Lyra star

We can compare the results presented here with the prototype of the RR Lyrae class, the RR Lyr itself, since it did not enter our calibration dataset due to its location at low Galactic latitude ($b = +12.304$ deg, see criteria in Section 3). Using the *Gaia* DR3 zero-point corrected parallax, we derive a geometrical distance $d = 249.9 \pm 1.9$ pc (which is in agreement with distances derived by Bailer-Jones et al. 2021, with $d = 249.5 \pm 1.5$ pc). For comparison, the parallax measured by *Hipparcos* (van Leeuwen 2007) yielded a distance of $d = 300 \pm 63$ pc, and the distance obtained from the parallax measurement by the Hubble Space Telescope was $d = 266 \pm 9$ pc (Benedict et al. 2011). We used 3D extinction map (Green et al. 2019) to obtain a color excess $E(B - V) = 0.01$ mag⁵ toward the RR Lyr variable. We decided to compare the PMZ predicted distance to the RR Lyr star only for the K_s -band PMZ relations since it will mitigate the effects of reddening and K_s -band PMZ relations are highly numerous in the literature. Therefore, we used the 2MASS mean intensity magnitude, m_{K_s} , for the RR Lyr variable and corrected it for pulsation

⁵ Using Schlegel et al. (1998) 2D extinction map, we would obtain $E(B - V) = 0.1$ mag.

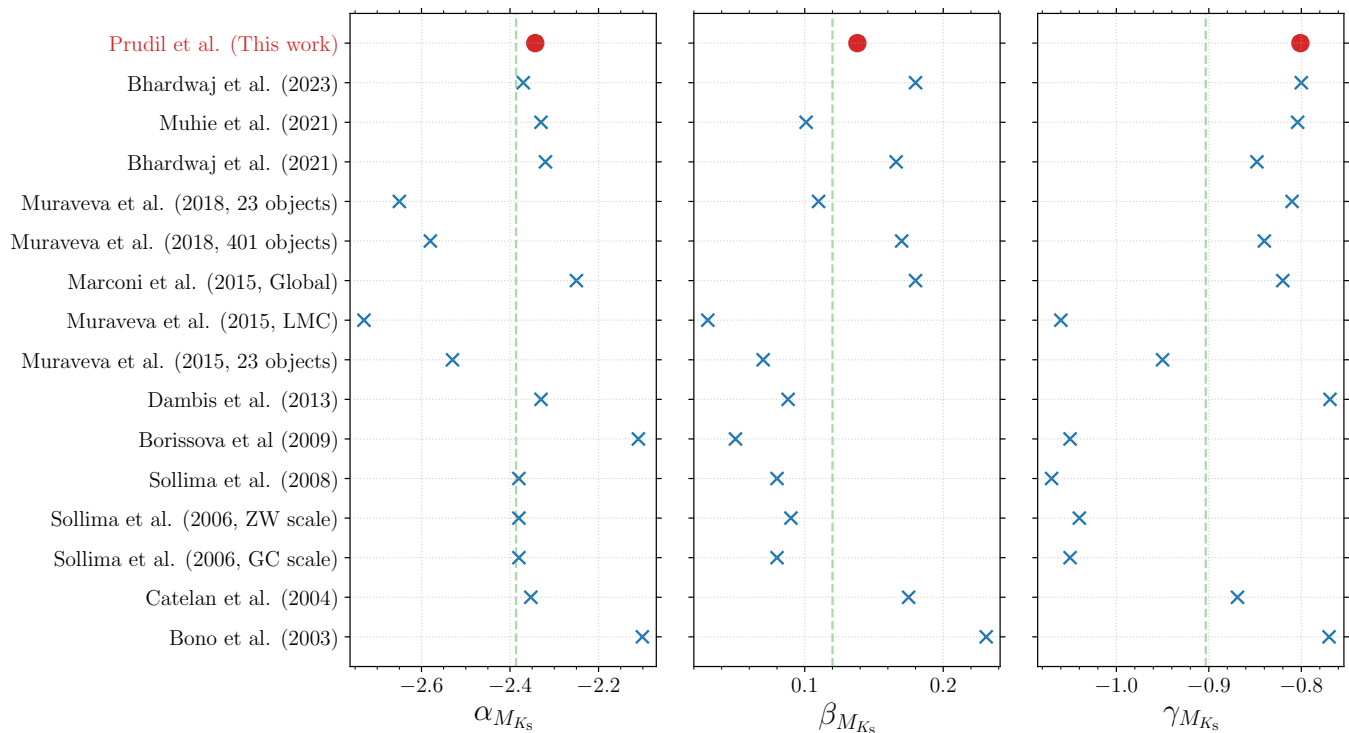


Fig. 5. Comparison of coefficients for K_s -passband PMZ relation across different studies (marked with blue crosses, e.g., Bono et al. 2003; Sollima et al. 2006, 2008; Borissova et al. 2009; Dambis et al. 2013; Muraveva et al. 2015; Bhardwaj et al. 2021; Muhie et al. 2021; Bhardwaj et al. 2023). Coefficients derived in this work are marked with red points. The Green dashed line represents the average of coefficients from previous studies.

motion using photometric templates from Braga et al. (2019). As ephemerides for the RR Lyr, we used data from the GEOS database (Le Borgne et al. 2007), with $M_0 = 2414921.7746$ day and $P = 0.566835616$ day (Szabó et al. 2014). We took into account that different PMZ relations considered different metallicity scales. Thus, for those that used the Zinn & West (1984) metallicity scale, we used $[\text{Fe}/\text{H}] = -1.37$ dex, while for other relations we used $[\text{Fe}/\text{H}] = -1.56$ dex.

In Table 2, we list a comparison of the distances for the RR Lyr between different PMZ relations (same as those used in Section 4.2). Over half of the PMZ relations overestimate the distance toward the RR Lyr. The scale of overestimation varies from four parsecs up to 26 pc among the different used PMZ laws. Distance differences under five parsecs can be explained by reddening corrections, metallicity variation, and partially by the *Gaia* parallax offset. The difference between the distance from our derived relation and *Gaia* is well within one sigma uncertainty of our distance even if we consider only errors on the observed properties (reddening, metallicity, mean intensity magnitude). Here is important to emphasize the correction of 2MASS mean magnitude for pulsation motion. If we had used the single epoch 2MASS K_s -band magnitude provided in the 2MASS catalog, we would overestimate the distance toward RR Lyr in nearly all compared PMZ relations. The distance from the PMZ relation would be shifted by approximately seven parsecs instead.

5. Conclusions

In this work, we calibrated empirical relations that describe the dependence of pulsation periods and metallicities on absolute magnitudes for both fundamental and first-overtone RR Lyrae variables. Our calibration sample was designed to accurately derive PMZ relations for surveys targeting dense stellar structures

Table 2. List of distances for the RR Lyrae star derived using various PMZ relations from the literature. The first column lists references for used PMZ relations. The second column represents the difference between the geometrical distance from *Gaia* parallax and the distance from the PMZ relation denoted in the third column.

| PMZ source | <i>Gaia</i> – PMZ [pc] | distance [pc] |
|--------------------------------------|---------------------------|------------------|
| Bono et al. (2003) | -25.6 | 275.5 |
| Catelan et al. (2004) | -19.2 | 269.1 |
| Sollima et al. (2006, GC scale) | -22.5 | 272.4 |
| Sollima et al. (2006, ZW scale) | -21.1 | 271.0 |
| Sollima et al. (2008) | -25.0 | 274.9 |
| Borissova et al. (2009) | -25.0 | 274.9 |
| Dambis et al. (2013) | 9.7 | 240.2 |
| Muraveva et al. (2015, 23 objects) | -4.0 | 253.9 |
| Muraveva et al. (2015, LMC) | -3.8 | 253.7 |
| Marconi et al. (2015, Global) | -17.3 | 267.2 |
| Muraveva et al. (2018a, 400 objects) | -4.2 | 254.1 |
| Muraveva et al. (2018a, 23 objects) | 10.5 | 239.4 |
| Bhardwaj et al. (2021) | -15.9 | 265.8 |
| Muhie et al. (2021) | 3.8 | 246.1 |
| Bhardwaj et al. (2023) | -11.3 | 261.2 |
| This work | -4.4 | 254.3 |

within the Galaxy. Our study focuses on the OGLE, *Gaia*, and VVV surveys that provide optical and near-infrared photometric observations for dozens of thousands of RR Lyrae stars in the Galactic disk, bulge, and in the Magellanic Clouds. Despite our calibration sample being smaller than the ones used in the past, we use a homogeneous metallicity scale that can be easily adapted for RR Lyrae stars in the aforementioned stellar systems.

Our calibration heavily relies on trigonometric parallaxes measured by the *Gaia* space telescope and the high-resolution metallicities on the CFCS metallicity scale introduced by Crestani

et al. (2021b). We considered uncertainties for all involved parameters in our Bayesian approach, including reddening, mean intensity magnitudes, pulsation periods, metallicities, and parallaxes. We also included a parameter for intrinsic scatter in the PMZ in all calibrated passbands to accurately estimate uncertainties in derived absolute magnitudes.

We tested our derived PMZ relations using systems with precise distances and with RR Lyrae stars with publicly available photometry. For optical G_{BP} , near-infrared I , J , and K_s passbands, our relations accurately estimate distance moduli to NGC 6121, NGC 5139, LMC, and SMC. In the case of the optical G_{BP} and G -bands for the globular cluster NGC 6121, we detect a significant offset in the derived distance modulus. The offset is mainly caused by the projected reddening and mostly disappears when we use 3D extinction maps toward NGC 6121.

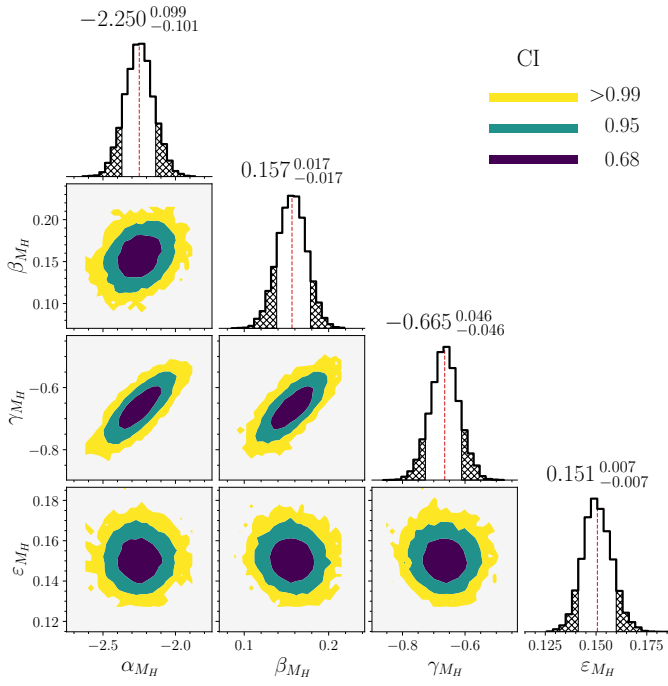
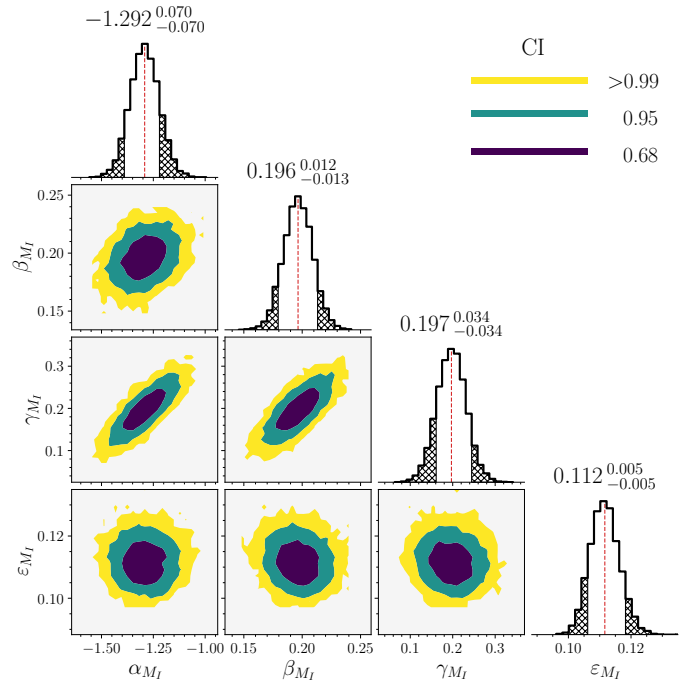
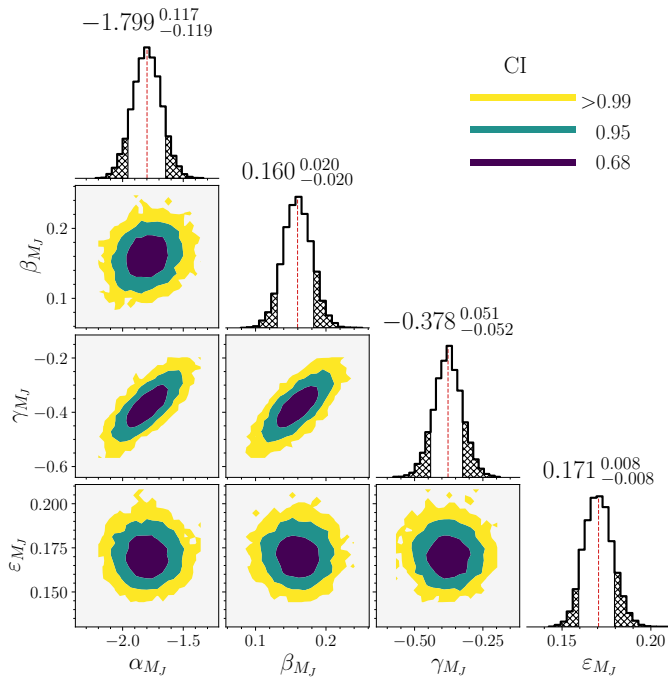
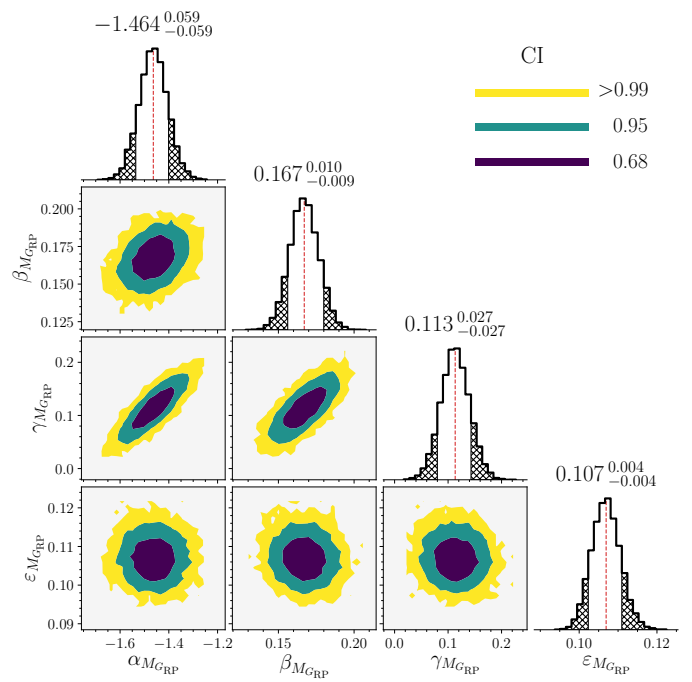
In addition, we compared our predicted K_s -band PMZ relation with previously published relations. Our period and metallicity parameters match well with the overall distribution of literature values (even with relations using a different metallicity scale). The zero-point parameter, on the other hand, matches with PMZ relations based on the *Gaia* parallaxes. Moreover, we tested assembled PMZ relation and our derived K_s -band PMZ to estimate the distance toward the prototype of RR Lyrae class, the RR Lyr. We found a good agreement between our derived distance value and distance from *Gaia*. Our derived PMZ relations will be used in the forthcoming papers to examine the structure and kinematics of the Galactic bulge.

Acknowledgements. Z.P. and A.J.K.H. acknowledge support by the Deutsche Forschungsgemeinschaft (DFG, German Research Foundation) – Project-ID 138713538 – SFB 881 (“The Milky Way System”, subprojects A03, A05, A11). AMK acknowledges support from grant AST-2009836 from the National Science Foundation. This work has made use of data from the European Space Agency (ESA) mission *Gaia* (<https://www.cosmos.esa.int/gaia>), processed by the *Gaia* Data Processing and Analysis Consortium (DPAC, <https://www.cosmos.esa.int/web/gaia/dpac/consortium>). Funding for the DPAC has been provided by national institutions, in particular the institutions participating in the *Gaia* Multilateral Agreement. This research made use of the following Python packages: *Astropy* (Astropy Collaboration et al. 2013, 2018), *dustmaps* (Green 2018), *emcee* (Foreman-Mackey et al. 2013), *IPython* (Pérez & Granger 2007), *Matplotlib* (Hunter 2007), *NumPy* (Harris et al. 2020), and *SciPy* (Virtanen et al. 2020).

References

- Astropy Collaboration, Price-Whelan, A. M., Sipőcz, B. M., et al. 2018, *AJ*, 156, 123
- Astropy Collaboration, Robitaille, T. P., Tollerud, E. J., et al. 2013, *A&A*, 558, A33
- Bailer-Jones, C. A. L., Rybizki, J., Fousneau, M., Demleitner, M., & Andrae, R. 2021, *AJ*, 161, 147
- Benedict, G. F., McArthur, B. E., Feast, M. W., et al. 2011, *AJ*, 142, 187
- Bhardwaj, A., Marconi, M., Rejkuba, M., et al. 2023, *ApJ*, 944, L51
- Bhardwaj, A., Rejkuba, M., de Grijs, R., et al. 2020, *AJ*, 160, 220
- Bhardwaj, A., Rejkuba, M., de Grijs, R., et al. 2021, *ApJ*, 909, 200
- Bono, G., Caputo, F., Castellani, V., & Marconi, M. 1996, *ApJ*, 471, L33
- Bono, G., Caputo, F., Castellani, V., et al. 2003, *MNRAS*, 344, 1097
- Borissova, J., Rejkuba, M., Minniti, D., Catelan, M., & Ivanov, V. D. 2009, *A&A*, 502, 505
- Braga, V. F., Dall’Ora, M., Bono, G., et al. 2015, *ApJ*, 799, 165
- Braga, V. F., Stetson, P. B., Bono, G., et al. 2016, *AJ*, 152, 170
- Braga, V. F., Stetson, P. B., Bono, G., et al. 2019, *A&A*, 625, A1
- Braga, V. F., Stetson, P. B., Bono, G., et al. 2018, *AJ*, 155, 137
- Cardelli, J. A., Clayton, G. C., & Mathis, J. S. 1989, *ApJ*, 345, 245
- Carretta, E., Bragaglia, A., Gratton, R., D’Orazi, V., & Lucatello, S. 2009, *A&A*, 508, 695
- Catelan, M. 2004, *ApJ*, 600, 409
- Catelan, M., Pritzl, B. J., & Smith, H. A. 2004, *ApJS*, 154, 633
- Chadid, M., Sneden, C., & Preston, G. W. 2017, *ApJ*, 835, 187
- Clementini, G., Ripepi, V., Garofalo, A., et al. 2022, arXiv e-prints, arXiv:2206.06278
- Crestani, J., Braga, V. F., Fabrizio, M., et al. 2021a, *ApJ*, 914, 10
- Crestani, J., Fabrizio, M., Braga, V. F., et al. 2021b, *ApJ*, 908, 20
- Cusano, F., Moretti, M. I., Clementini, G., et al. 2021, *MNRAS*, 504, 1
- Cutri, R. M., Skrutskie, M. F., van Dyk, S., et al. 2003, *VizieR Online Data Catalog*, II/246
- Dall’Ora, M., Storm, J., Bono, G., et al. 2004, *ApJ*, 610, 269
- Dambis, A. K. 2009, *MNRAS*, 396, 553
- Dambis, A. K., Berdnikov, L. N., Kniazev, A. Y., et al. 2013, *MNRAS*, 435, 3206
- Dékány, I., Grebel, E. K., & Pojmański, G. 2021, *ApJ*, 920, 33
- Dékány, I., Minniti, D., Catelan, M., et al. 2013, *ApJ*, 776, L19
- Du, H., Mao, S., Athanassoula, E., Shen, J., & Pietrukowicz, P. 2020, *MNRAS*, 498, 5629
- Fabrizio, M., Braga, V. F., Crestani, J., et al. 2021, *ApJ*, 919, 118
- Fiorentino, G., Contreras Ramos, R., Tolstoy, E., Clementini, G., & Saha, A. 2012, *A&A*, 539, A138
- For, B.-Q., Sneden, C., & Preston, G. W. 2011, *ApJS*, 197, 29
- Foreman-Mackey, D., Hogg, D. W., Lang, D., & Goodman, J. 2013, *PASP*, 125, 306
- Gaia Collaboration, Babusiaux, C., van Leeuwen, F., et al. 2018, *A&A*, 616, A10
- Gaia Collaboration, Prusti, T., de Bruijne, J. H. J., et al. 2016, *A&A*, 595, A1
- Gaia Collaboration, Vallenari, A., Brown, A. G. A., et al. 2022, arXiv e-prints, arXiv:2208.00211
- Garofalo, A., Delgado, H. E., Sarro, L. M., et al. 2022, *MNRAS*, 513, 788
- Graczyk, D., Pietrzyński, G., Thompson, I. B., et al. 2020, *ApJ*, 904, 13
- Green, G. 2018, *The Journal of Open Source Software*, 3, 695
- Green, G. M., Schlafly, E., Zucker, C., Speagle, J. S., & Finkbeiner, D. 2019, *ApJ*, 887, 93
- Harris, C. R., Millman, K. J., van der Walt, S. J., et al. 2020, *Nature*, 585, 357–362
- Hunter, J. D. 2007, *Computing in Science & Engineering*, 9, 90
- Iben, I., J. & Huchra, J. 1971, *A&A*, 14, 293
- Jacyszyn-Dobrzaniecka, A. M., Mróz, P., Kruszyńska, K., et al. 2020, *ApJ*, 889, 26
- Jacyszyn-Dobrzaniecka, A. M., Skowron, D. M., Mróz, P., et al. 2017, *Acta Astron.*, 67, 1
- Jayasinghe, T., Kochanek, C. S., Stanek, K. Z., et al. 2018, *MNRAS*, 477, 3145
- Jaynes, E. T. 1968, *IEEE Transactions on Systems Science and Cybernetics*, 4, 227
- Kunder, A., Pérez-Villegas, A., Rich, R. M., et al. 2020, *AJ*, 159, 270
- Kunder, A., Rich, R. M., Koch, A., et al. 2016, *ApJ*, 821, L25
- Layden, A. C., Tiede, G. P., Chaboyer, B., Bunker, C., & Smitka, M. T. 2019, *AJ*, 158, 105
- Le Borgne, J. F., Paschke, A., Vandenbroere, J., et al. 2007, *A&A*, 476, 307
- Lindgren, L., Bastian, U., Biermann, M., et al. 2021, *A&A*, 649, A4
- Longmore, A. J., Fernley, J. A., & Jameson, R. F. 1986, *MNRAS*, 220, 279
- Marconi, M., Bono, G., Pietrinferni, A., et al. 2018, *ApJ*, 864, L13
- Marconi, M., Coppola, G., Bono, G., et al. 2015, *ApJ*, 808, 50
- Martínez-Vázquez, C. E., Stetson, P. B., Monelli, M., et al. 2016, *MNRAS*, 462, 4349
- Martínez-Vázquez, C. E., Vivas, A. K., Gurevich, M., et al. 2019, *MNRAS*, 490, 2183
- Minniti, D., Lucas, P. W., Emerson, J. P., et al. 2010, *New A*, 15, 433
- Molnár, L., Bódi, A., Pál, A., et al. 2022, *ApJS*, 258, 8
- Molnar, T. A., Sanders, J. L., Smith, L. C., et al. 2022, *MNRAS*, 509, 2566
- Muhie, T. D., Dambis, A. K., Berdnikov, L. N., Kniazev, A. Y., & Grebel, E. K. 2021, *MNRAS*, 502, 4074
- Muraveva, T., Delgado, H. E., Clementini, G., Sarro, L. M., & Garofalo, A. 2018a, *MNRAS*, 481, 1195
- Muraveva, T., Palmer, M., Clementini, G., et al. 2015, *ApJ*, 807, 127
- Muraveva, T., Subramanian, S., Clementini, G., et al. 2018b, *MNRAS*, 473, 3131
- Neeley, J. R., Marengo, M., Bono, G., et al. 2017, *ApJ*, 841, 84
- Neeley, J. R., Marengo, M., Bono, G., et al. 2015, *ApJ*, 808, 11
- Neeley, J. R., Marengo, M., Freedman, W. L., et al. 2019, *MNRAS*, 490, 4254
- Nemec, J. M., Cohen, J. G., Ripepi, V., et al. 2013, *ApJ*, 773, 181
- Netzel, H. & Smolec, R. 2022, *MNRAS*, 515, 3439
- Netzel, H., Smolec, R., & Moskalik, P. 2015, *MNRAS*, 447, 1173
- Pérez, F. & Granger, B. E. 2007, *Computing in Science and Engineering*, 9, 21
- Petersen, J. O. 1986, *A&A*, 170, 59
- Pietrukowicz, P., Kozłowski, S., Skowron, J., et al. 2015, *ApJ*, 811, 113
- Pietrzyński, G., Graczyk, D., Gialenne, A., et al. 2019, *Nature*, 567, 200
- Pojmański, G. 1997, *Acta Astron.*, 47, 467
- Prudil, Z., Dékány, I., Catelan, M., et al. 2019a, *MNRAS*, 484, 4833
- Prudil, Z., Dékány, I., Grebel, E. K., et al. 2019b, *MNRAS*, 487, 3270
- Sarajedini, A., Barker, M. K., Geisler, D., Harding, P., & Schommer, R. 2006, *AJ*, 132, 1361
- Sarajedini, A., Mancone, C. L., Lauer, T. R., et al. 2009, *AJ*, 138, 184
- Savino, A., Weisz, D. R., Skillman, E. D., et al. 2022, arXiv e-prints, arXiv:2206.02801
- Schlafly, E. F. & Finkbeiner, D. P. 2011, *ApJ*, 737, 103
- Schlegel, D. J., Finkbeiner, D. P., & Davis, M. 1998, *ApJ*, 500, 525
- Shappee, B. J., Prieto, J. L., Grupe, D., et al. 2014, *ApJ*, 788, 48

- Skarka, M., Prudil, Z., & Jurcsik, J. 2020, *MNRAS*, 494, 1237
- Skowron, D. M., Soszyński, I., Udalski, A., et al. 2016, *Acta Astron.*, 66, 269
- Skrutskie, M. F., Cutri, R. M., Stiening, R., et al. 2006, *AJ*, 131, 1163
- Smolec, R., Soszyński, I., Udalski, A., et al. 2015, *MNRAS*, 447, 3756
- Snedden, C., Preston, G. W., Chadid, M., & Adamów, M. 2017, *ApJ*, 848, 68
- Sollima, A., Cacciari, C., Arkharov, A. A. H., et al. 2008, *MNRAS*, 384, 1583
- Sollima, A., Cacciari, C., & Valenti, E. 2006, *MNRAS*, 372, 1675
- Soszyński, I., Udalski, A., Szymański, M. K., et al. 2016, *Acta Astron.*, 66, 131
- Stetson, P. B., Braga, V. F., Dall’Ora, M., et al. 2014, *PASP*, 126, 521
- Szabó, R., Benkő, J. M., Paparó, M., et al. 2014, *A&A*, 570, A100
- Szabó, R., Kolláth, Z., Molnár, L., et al. 2010, *MNRAS*, 409, 1244
- Szczygieł, D. M., Pojmański, G., & Pilecki, B. 2009, *Acta Astron.*, 59, 137
- Tatton, B. L., van Loon, J. T., Cioni, M. R. L., et al. 2021, *MNRAS*, 504, 2983
- Udalski, A., Szymański, M. K., & Szymański, G. 2015, *Acta Astron.*, 65, 1
- van Leeuwen, F. 2007, *A&A*, 474, 653
- Vasiliev, E. & Baumgardt, H. 2021, *MNRAS*, 505, 5978
- Virtanen, P., Gommers, R., Oliphant, T. E., et al. 2020, *Nature Methods*, 17, 261
- Watson, C. L., Henden, A. A., & Price, A. 2006, *Society for Astronomical Sciences Annual Symposium*, 25, 47
- Zinn, R. & West, M. J. 1984, *ApJS*, 55, 45


 Fig. A.1. Same as Fig. 2 but for the H -band.

 Fig. A.3. Same as Fig. 2 but for the I -band.

 Fig. A.2. Same as Fig. 2 but for the J -band.

 Fig. A.4. Same as Fig. 2 but for the G_{RP} -band.

Appendix A: Additional figures

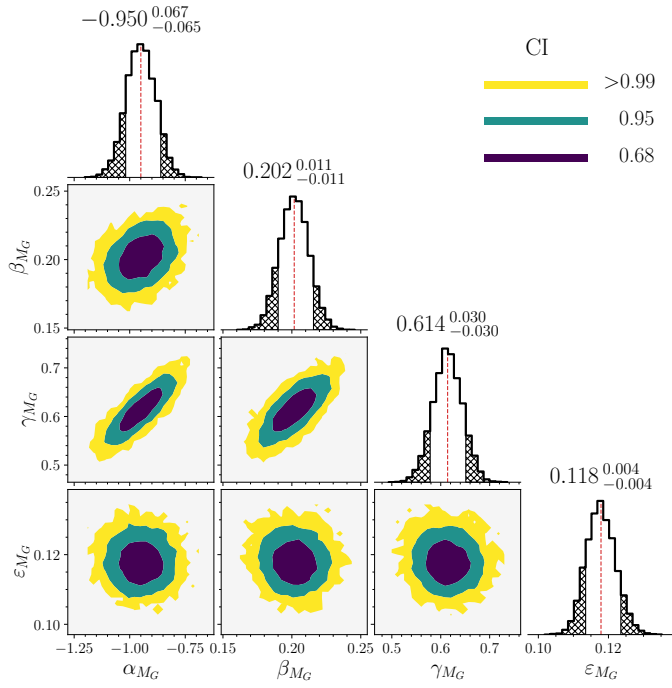


Fig. A.5. Same as Fig. 2 but for the G-band.

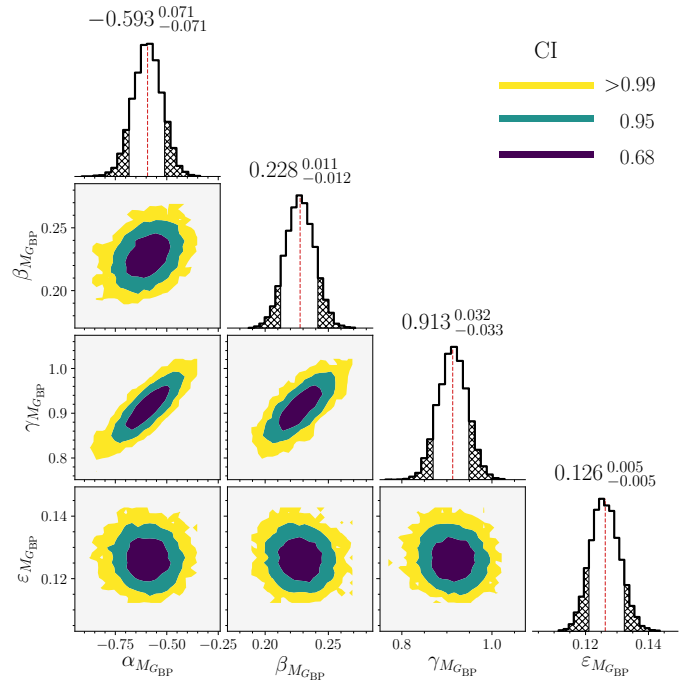


Fig. A.7. Same as Fig. 2 but for the G_{BP} -band.

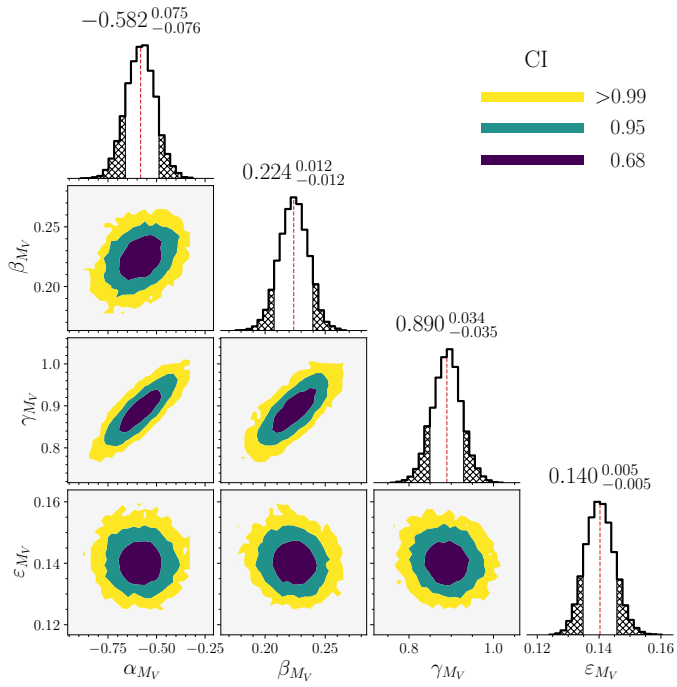


Fig. A.6. Same as Fig. 2 but for the V-band.

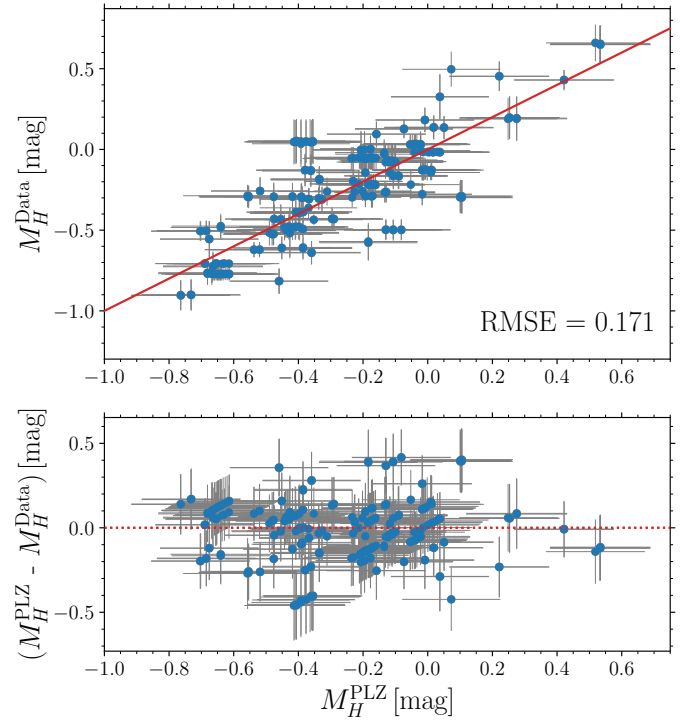


Fig. A.8. Same as Fig. 3 but for the J-band.

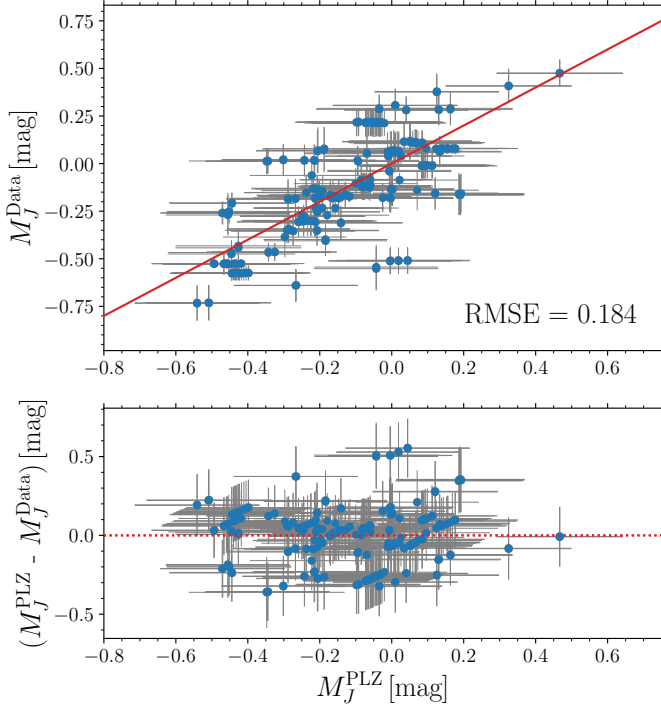


Fig. A.9. Same as Fig. 3 but for the J -band.

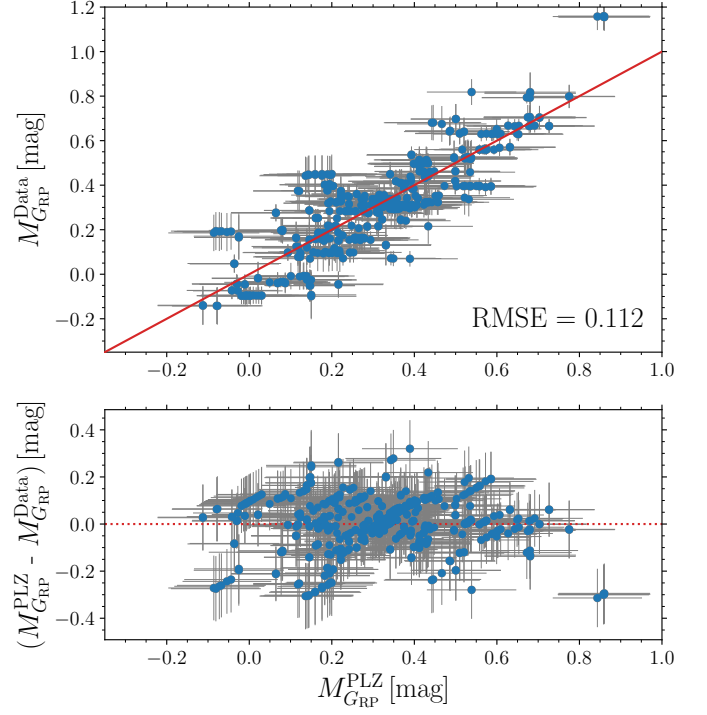


Fig. A.11. Same as Fig. 3 but for the G_{RP} -band.

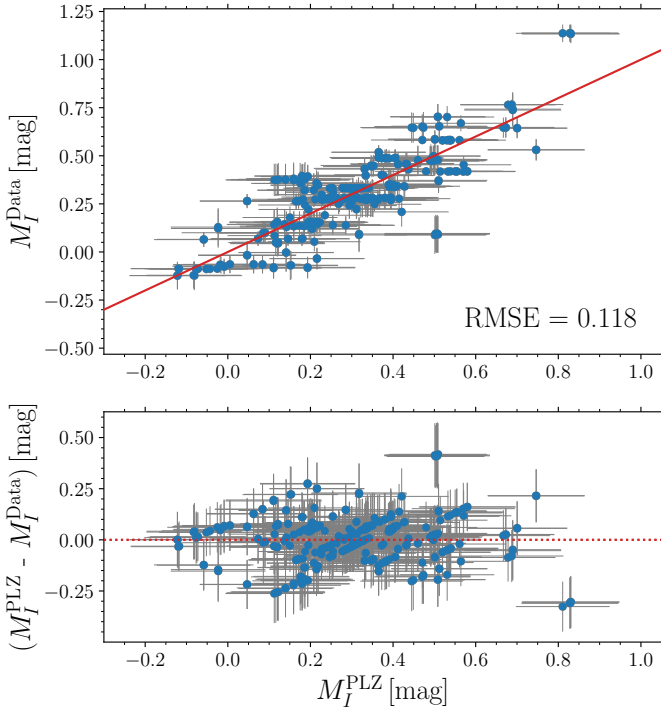


Fig. A.10. Same as Fig. 3 but for the I -band.

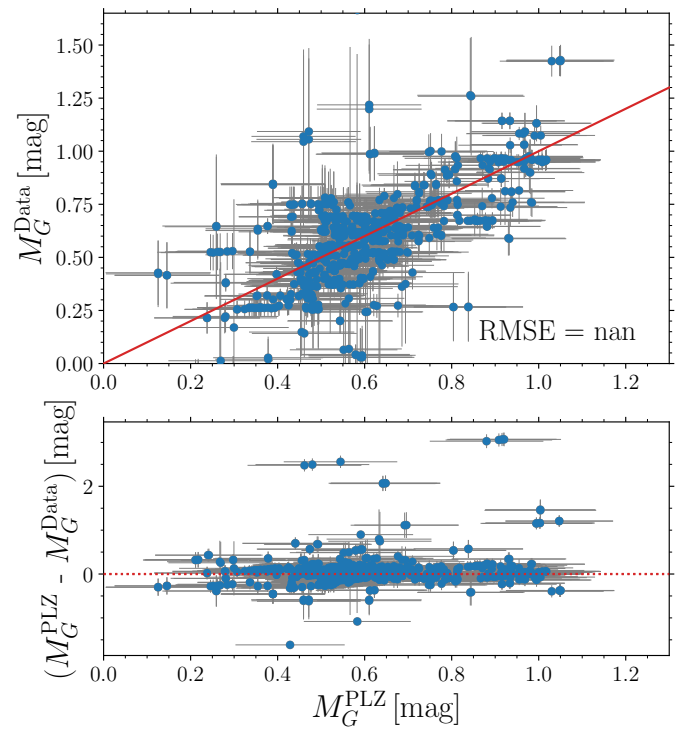


Fig. A.12. Same as Fig. 3 but for the G -band.

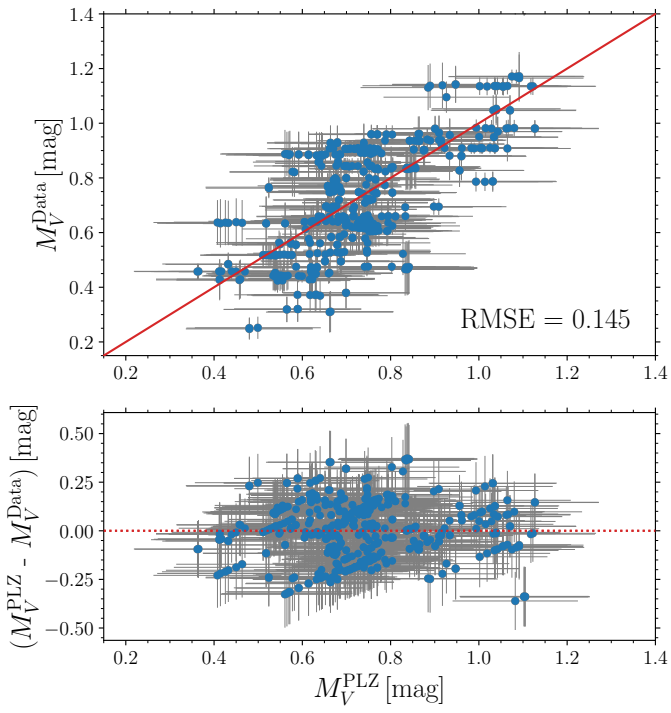


Fig. A.13. Same as Fig. 3 but for the V-band.

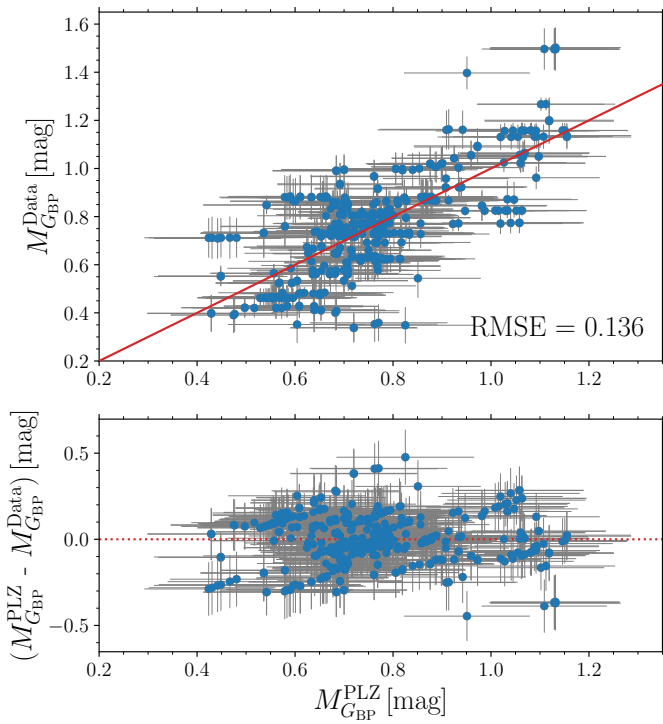


Fig. A.14. Same as Fig. 3 but for the G_{BP} -band.